TÜBİTAK

Turkish Journal of Earth Sciences

http://journals.tubitak.gov.tr/earth/

Research Article

Turkish J Earth Sci
(2020) 29: 1004-1016

doi:10.3906/yer-2003-11

Determination of deformations by using the PSI technique at a common dump site of three different open-pit marble mines in Turkey

Fatih POYRAZ[1,*], **Yavuz GÜL**[2], **Burakhan DUYMAZ**[1]

[1]Department of Geomatics Engineering, Faculty of Engineering, Sivas Cumhuriyet University, Sivas, Turkey
[2]Department of Mining Engineering, Faculty of Engineering, Sivas Cumhuriyet University, Sivas, Turkey

Received: 17.03.2020 • **Accepted/Published Online:** 26.07.2020 • **Final Version:** 04.09.2020

Abstract: Slopes are formed to carry out mining activities such as stripping, ore production, transportation, and waste management in open-pit mines. The instability of slopes is a potential source of risks for mine safety. An unexpected slope failure may damage people, buildings, and equipment in the immediate area. Moreover, it leads to the disruption of mining production and an increase in production cost. For this reason, the regular examination and systematic monitoring of slopes should be performed to determine the early warning signs of failure. Thus, it may be possible to reach acceptable risk levels and to plan and implement the necessary safety measures. In this study, deformations at a common dump site of three different open-pit marble mines located in Eliktekke region of Amasya province (Turkey) were investigated by the permanent scatterer interferometry (PSI) technique using satellite radar images. The results obtained from the PSI technique were compared with global navigation satellite system (GNSS) and unmanned aerial vehicle (UAV) photogrammetry results which had been conducted by Hastaoğlu et al. (2019) in the same study area. Velocities in the satellite line of sight (LOS) direction approaching –70 mm/month were determined from the PSI results of this dump site. Although the obtained results provided the overall coherence at this site, different results were found from GNSS and UAV photogrammetry in the areas where step geometry (height, width, inclination) changed along with the ongoing dumps and frequently changing surface topography due to dumping. While deformations occurring in slow motion and in a long time could be revealed by the PSI technique, displacements that occurred instantly and in a short time could not be determined. This study showed the detectability of surface deformations in open-pit mines by the PSI technique and problems that might be encountered during the analysis stage.

Key words: Landslide, deformation, PSI, surface mining, slope failure

1. Introduction

Surface deformations resulting from mining activities at mining sites are generally monitored by various methods, such as global navigation satellite system (GNSS) receivers, geometric leveling, terrestrial laser imaging detection and ranging (LIDAR), and unmanned aerial vehicle (UAV) photogrammetry. Among these methods, the GNSS technique and the geometric leveling method produce precise point values. Point deformations could also be measured using geotechnical instruments such as crackmeters, inclinometers, extensometers, piezometers, and microseismic geophones (Jarosz and Wanke, 2004). Techniques for point-based deformation detection, such as inclinometer, extensometer and GNSS, require tracking of numerous points to monitor whole of the large scale mine site and involve high costs due to sophisticated data management (Jarosz and Wanke, 2004). These point measurements are often insufficient for the assessment of the kinematics and behaviors of displacements dependent on large landslides characterized by complex movements (Colesanti et al., 2005; Kristensen et al., 2012; Jakóbczyk et al., 2015). Although terrestrial LIDAR and UAV photogrammetry allow for the determination of areal deformations, they produce results that vary according to the properties of the equipment used. Airborne LIDAR data and imagery are safe, accurate, and able to achieve a valuable top-view. However, the extremely high cost associated with the use of aircraft and its time-consuming nature makes this strategy an impractical solution, especially for investigations of small areas (Al-Rawabdeh et al., 2016). UAV photogrammetry has been widely used in deformation monitoring studies in recent years. This method has been used in many studies, such as monitoring tectonic movements (Deffontaines et al., 2016), determining deformations at mine sites (Tong et al., 2015; Hastaoğlu et al., 2019; Ren et al., 2019), monitoring landslides (Niethammer et al., 2012; Peppa et al., 2017; Eker et al., 2018), and it has been emphasized that valuable

* Correspondence: fpoyraz@gmail.com

data could be produced with UAV, but improvements were needed to increase for accuracy. The ground-based synthetic aperture radar (GB-SAR) technique is also used at many mine sites. This technique is limited due to the linear observation feature of its system, especially vertical displacement observations in flat areas (Ferrigno et al., 2007). In recent years, methods such as interferometric synthetic aperture radar (InSAR), which allow for the determination of surface deformations and movements, especially in large areas, and use satellite data, have begun to come to the forefront. InSAR is one of the techniques that is applied for the analysis of surface deformation processes using satellite images.

With the InSAR method, a digital elevation model (DEM) of the studied region can be created by using the phase information in the interferogram, and surface deformations in centimeters or below centimeters can be determined in the satellite line of sight (LOS) direction. Furthermore, with the permanent scatterer interferometry (PSI) technique, which is the most used among the InSAR methods, movements occurring on the surface as a result of events such as earthquakes, volcanoes, glaciers, and landslides can be determined in the LOS direction, and deformations can be revealed areally (Colesanti et al., 2003a; Colesanti et al., 2003b; Canuti et al., 2004; Colesanti and Wasowski, 2004; Ferretti et al., 2005).

There are many studies successfully observing displacements that occur in surface mines using the InSAR data. Mora et al. (2013) successfully observed the displacements of production slopes of an open-pit coal mine located in the northwest of Spain by the PSI technique using the images of the years 2008–2012 obtained from the TerraSAR-X satellite, and they performed slope stability analysis by considering the displacement values. Meisina et al. (2006) successfully performed the determination and monitoring of displacement in Oltrepo Pavese in Northern Italy, which is considered as a complex geological and structural area, using the PSI technique. Pinto et al. (2014) effectively applied the PSI technique to an open-pit manganese mine. Pinto et al. (2015) indicated that high accuracy could be achieved in the case of long-term displacement monitoring using the PSI technique, without the need for terrestrial measuring instruments and field studies, in open-pit mining areas, dump sites, and regions around open-pit mines.

Graniczny et al. (2015) performed a detailed InSAR analysis in the Upper Silesian Coal Basin in Poland. They applied both the differential interferometry synthetic aperture radar (DInSAR) and PSI techniques for different data sets such as ERS1/2, Envisat, ALOS, and TerraSAR-X. With these techniques, they associated the topographic elevations in the field, depending on underground water.

Bozzano et al. (2015) associated the spatial and temporal evolution of a collapse process monitored in the Acque Albule Basin (Italy), which is an area of approximately 30 km^2. The authors performed the advanced DInSAR analysis of ERS and Envisat satellite images taken in 1992. They also indicated that groundwater level changes triggered the collapse in the area, using the historical data set of radar images with the PSI technique.

Paradella et al. (2015) monitored surface deformations in open-pit iron mines located in Carajás province (Amazon Region) by the PSI technique using 33 TERRASAR-X images. They said that the approach was effective in monitoring deformations in the region. But on the other hand, they indicated that they could not determine deformations which developed in a fast and sudden way by this method. In the study on the determination of deformations at mining sites by the PSI technique, Temporim et al. (2017) indicated that intensive surface movements affected the results negatively due to mining processes.

Perski et al. (2009) investigated the potential relationship between underground mining activities in the Wieliczka salt mine located on the edge of the Carpathian mountains in Poland and landslide events occurring on the surface. In their study, they performed the DInSAR and PSI analyses using ERS-1 and ERS-2 images in order to separate the observed field deformations into three different types. They indicated that slow-motion subsidences occurring on the surface due to the spaces formed from underground mining could be easily determined while the rapid field deformation caused by water intake could not be determined by InSAR analysis.

In open-pit mining activities, it is necessary to monitor deformations occurring on the surface to ensure the safety of people and buildings, the continuity of production, and to determine whether these deformations have reached the critical risk value. Therefore, the effects to be caused by surface deformations should be examined through periodic observations at frequent intervals, and it is necessary to create unique behavior models according to the geomechanical properties of the field (Akcin et al., 2007).

Hastaoğlu et al. (2019) monitored deformations at the same study area using the UAV photogrammetry and GNSS technique. The movement values of approximately 2 mm/month –70 mm/month horizontally and approximately 3 mm/month and –100 mm/month vertically were obtained by using the GNSS method and UAV photogrammetry at the dump site. Furthermore, there are 3 m horizontal and 1 m vertical sudden displacements at the deformation point D35.

The aim of this study was to determine the possible landslides or massive displacements that may occur in and/or around the excavation area or at the dump sites of mines by the PSI technique. A common dump site of three different open-pit marble mines located in Eliktekke

village of Amasya province was selected as the study area. Surface deformations were determined by the PSI technique, obtaining the Sentinel-1A images in a way to cover the same time periods for the dump site studied in the article of Hastaoğlu et al. (2019), and the success of the technique was measured.

Although one of the most commonly used techniques for the determination of deformations with satellite images is the DInSAR method, the PSI technique was preferred in this study. As the temporal difference between the images used in the DInSAR increases, the coherence of the images decreases, and thus, displacements can not be determined precisely. The PSI technique, which was developed to reduce this effect, can produce much more precise results in a time series by using many image sets compared to the DInSAR technique (Ferretti et al., 2001).

2. Materials and methods

2.1. Study area

The study area is the common dump site of three different marble mines located in Eliktekke village of Amasya province (Figure 1). This site is approximately 800 m in width and 900 m in length and covers an area of approximately 70 ha. The maximum height difference was determined to be 145 m. The base topography of the dump site has a slope of about 9°, and the overall slope angle at the benched dump site varies between 8°–18° (Gül et al., 2020). In the study area, displacements and velocity values had been previously obtained (Hastaoğlu et al., 2019) by the GNSS method and UAV photogrammetry with a total of 49 deformation plates.

2.2. Data set

Sentinel-1A images in the IW mode used in this study are open access, and they were obtained from the European Space Agency (ESA). The IW mode supports a single and double polarization option. Sentinel data images having a wide range of 250 km and medium spatial resolution (5 m ′ 20 m along the ground-range and azimuth directions) can be used in medium resolution applications. Within the scope of this study, a total of 28 images, including 14 images in the descending orbits and 14 images in the ascending orbits, were evaluated between May 2018 and October 2018, with a temporal resolution of 12 days (Table 1). This time interval was determined to cover the measurement periods in the study carried out by Hastaoğlu et al. (2019). Especially, the images were selected in a wider range due to the landslide occurred in July (point D35) which was also indicated in the study of Hastaoğlu et al. (2019).

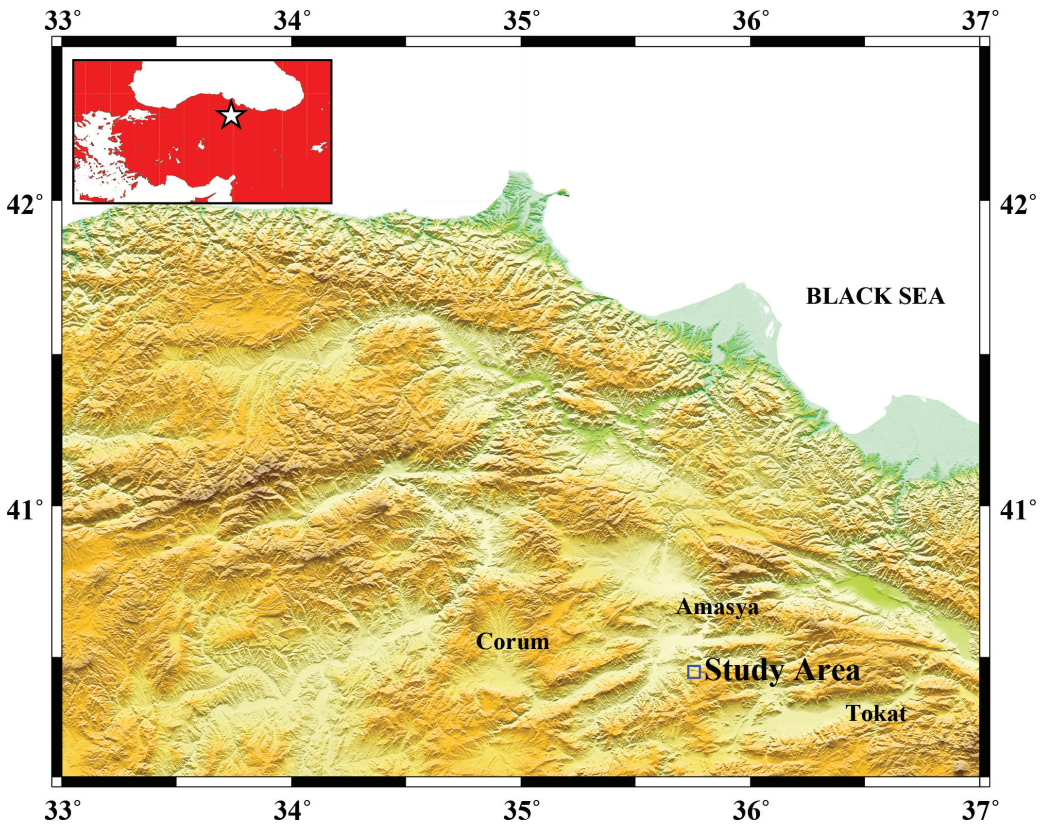

Figure 1. Study area.

Table 1. Perpendicular baseline and temporal baselines of Sentinel-1A (14 track/ascending and 94 track/descending) images used for PSI analysis.

Image ID	14 Frame			94 Frame		
	Date	Bperp (m)	Btemp (days)	Date	Bperp (m)	Btemp (days)
1	22.08.2018	0	0	28.08.2018	0	0
2	18.05.2018	–5.69	96	24.05.2018	–31.81	96
3	30.05.2018	46.55	84	05.06.2018	–92.80	84
4	11.06.2018	9.11	72	17.06.2018	–24.45	72
5	23.06.2018	–7.02	60	29.06.2018	37.87	60
6	05.07.2018	35.64	48	11.07.2018	14.14	48
7	17.07.2018	–25.10	36	23.07.2018	–13.86	36
8	29.07.2018	48.69	24	04.07.2018	–44.18	24
9	10.08.2018	69.33	12	16.08.2018	–37.89	12
10	03.09.2018	–108.84	–12	09.09.2018	40.45	–12
11	15.09.2018	–41.74	–24	21.09.2018	10.91	–24
12	27.09.2018	25.90	–36	03.10.2018	–78.81	–36
13	09.10.2018	65.49	–48	15.10.2018	31.75	–48
14	21.10.2018	22.05	–60	27.10.2018	54.42	–60

2.3. Data processing

Within the scope of data processing studies, the results were reached in two different stages with two different software packages. In the first stage, the Sentinel Application Platform (SNAP) software suitable for open access and supported and developed by the ESA was used. Satellite radar images in the Sentinel-1A format were used as the input data in this software. Sentinel images consist of 3 sections (IW1, IW2, and IW3). Initially, the splitting process is applied to Sentinel images one by one. Subsequently, sensitive orbit files are loaded on the images to applied splitting, then the master image is selected for the coregistration of Sentinel radar images. The image that can show the best coherence in a way to form the base distance of radar images among themselves, the time of images, and their combination is called the master image. The sections (IW1, IW2, and IW3), in which Sentinel 1A radar data are formed, consist of 9 subsections, and there are spaces between them. The deburst process step is performed to remove these band spaces. After these operations, if required, the image is reduced by making a subset according to the working region. Master and slave images are used in this stage. Interferograms are formed according to the phase differences between master and slave images. In the last stage, the topographic effect in interferograms is removed. Topographic phase is simulated and subtracted using the SRTM 3 arc-seconds digital terrain model (DTM), using the automatic downloaded option in SNAP (topographic phase removal). The interferograms obtained from this process were used as input data for the stanford method for PS software (StaMPS) choosing the best permanent scatterer (PS) points. Then velocities in the LOS direction were obtained from the time series of these points. Hooper et al. (2007) developed the StaMPS method in the deformation analysis of crust motions by addressing the PSI technique with a different approach. This method uses the spatial correlation of the interferometric phase in finding the pixels with a low phase change to perform analysis in all field types, whether or not there are significant objects such as buildings. The coherence maps of interferograms are used to determine the fixed target points. The number of SAR images is recommended to be higher than 12 in order to increase the number of PS points (Hooper, 2007). The amplitude values of a pixel in each image form the time series. The pixels which are unaffected by the irregular geometrical and temporal correlation and having a series of constant amplitude values are selected as PS points. The error between current topography and the used DTM is determined, and then the phase unwrapping process is performed by removing orbital errors. In the final stage, the deformation phase is sperated from the atmosphere and noise phases by the application of spatial and temporal filters (Hooper et al., 2018). The workflow diagram covering SNAP and StaMPS processes is presented in Figure 2.

The evaluation of the study area with satellite radar images was performed with Sentinel-1A images directed and used by the European Space Agency. Fourteen

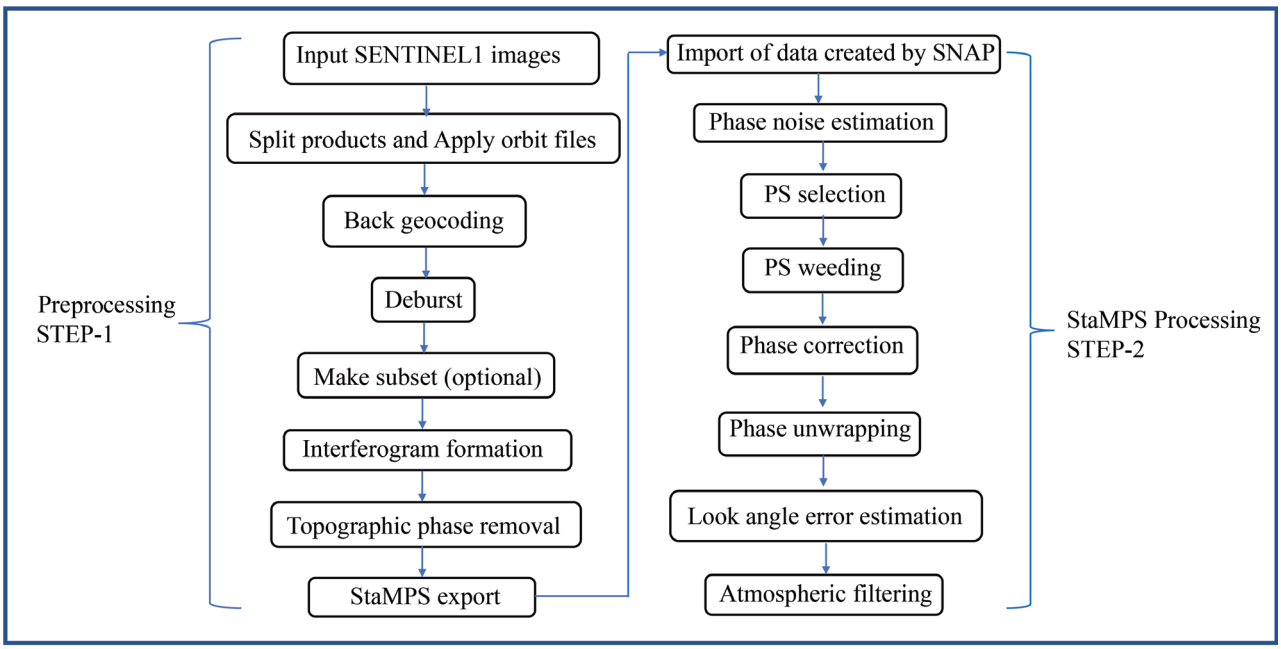

Figure 2. Workflow diagram for the processing of satellite radar images.

ascending (14 track number) and fourteen descending (94 track number) satellite images were used. Among these images, the master image (descending and ascending) required for the PSI technique was determined through the SNAP program, and the processes were continued upon it (Figure 2). The temporal and spatial distributions of the master images used in the evaluation according to the other descending and ascending satellite images are presented in Figure 3.

The movements in the satellite line of sight direction were calculated from the relative motion obtained by evaluating all PS points in the related track number (Figures 4 and 6). When the movements of the images with 14 and 94 track numbers in the LOS direction were examined, it was observed that collapses occurred in the middle section of the dump site. As a result of the evaluation of the images with 14 track number, the maximum collapse value in the LOS direction was approximately –50 mm/month, and the upheaval value was approximately 40 mm/month. In the evaluation of the images with 94 track number, it was determined that the maximum collapse value in the LOS direction was approximately –60 mm/month, and the upheaval value was 40 mm/month. Furthermore, the standard deviations of the PS points are presented in Figures 5 and 7.

Hastaoğlu et al. (2019) determined that deformations of the region ranged from 2 mm/month –70 mm/month horizontally and 3 mm/month –100 mm/month vertically, except for point number D35. The biggest deformation was found at point number D35, to be approximately 3 m

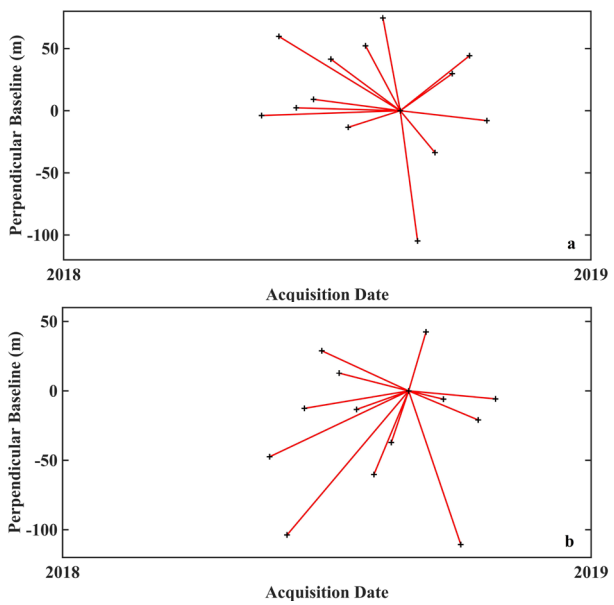

Figure 3. (a) Temporal and spatial distribution of 14 Sentinel-1A images with an ascending feature and 14 track number according to the master image, (b) temporal and spatial distribution of 14 Sentinel-1A images with a descending feature and 94 track number according to the master image (Red lines indicate interferogram pairs).

in the horizontal direction / 1 m in the vertical direction (Table 2). For comparasion of PSI results in this study, the horizontal and vertical velocities found by Hastaoğlu

Table 2. Movement velocities of 35 points (Hastaoğlu et al., 2019) and LOS velocities calculated from these velocities.

Site ID	GNSS			Ascending	Descending	UAV			Ascending	Descending
	Vn (mm/mo)	Ve (mm/mo)	Vup (mm/mo)	V_{LOS} (mm/mo)	V_{LOS} (mm/mo)	Vn (mm/mo)	Ve (mm/mo)	Vup (mm/mo)	V_{LOS} (mm/mo)	V_{LOS} (mm/mo)
D1	8.65	–9.01	–7.76	–1.05	–12.58	2.23	–0.97	–14.88	–10.90	–12.33
D2	32.09	–4.11	–11.05	–9.28	–14.62	21.26	–2.10	–8.90	–7.75	–10.51
D3	26.20	–3.02	–5.41	–5.06	–8.94	13.15	1.43	1.65	–1.12	0.73
D4	60.80	2.78	–21.36	–24.71	–21.40	40.41	3.97	–9.55	–14.26	–9.31
D5	28.63	1.00	–12.22	–13.07	–11.94	17.24	–2.95	–1.45	–1.11	–4.86
D6	10.89	2.46	–13.94	–13.35	–10.40	2.53	2.74	17.53	11.24	14.96
D7	2.37	–1.22	–3.58	–2.19	–3.79	–5.00	9.13	–0.56	–5.74	5.84
D8	–2.09	–3.60	–4.64	–0.97	–5.61	–8.16	3.34	–6.93	–6.50	–2.35
D9	–2.66	0.34	–7.49	–5.60	–5.27	–12.82	4.21	–18.84	–15.57	–10.48
D10	3.46	–4.01	–2.55	0.26	–4.86	–5.94	2.91	14.74	9.96	13.84
D11	–1.42	0.25	2.35	1.78	2.12	–6.39	1.63	5.41	3.76	5.89
D12	2.36	3.66	–12.75	–12.28	–7.79	–0.53	8.35	–27.13	–25.87	–15.62
D13	2.42	–2.33	0.68	1.75	–1.20	–4.12	12.38	–22.00	–24.18	–8.74
D14	2.28	0.33	–3.98	–3.48	–3.11	–0.26	15.73	10.11	–2.42	17.69
D15	3.29	2.64	–1.27	–3.02	0.32	–4.38	7.78	4.45	–1.14	8.79
D16	–0.27	–1.53	–5.02	–2.79	–4.80	–0.19	3.14	0.18	–1.86	2.13
D17	–6.66	5.30	–14.64	–13.77	–7.23	–22.95	5.76	–7.90	–7.15	0.04
D18	1.57	–2.67	–12.15	–7.67	–11.21	0.17	6.22	–13.75	–14.44	–6.72
D19	5.55	–7.21	–12.99	–5.82	–15.15	1.40	2.24	–2.50	–3.49	–0.68
D21	–0.99	–5.22	–12.97	–6.36	–13.17	–6.29	2.66	–5.05	–4.84	–1.53
D22	5.88	8.36	–33.48	–31.40	–21.21	–20.70	15.55	–19.60	–22.56	–3.08
D23	8.17	–11.39	–70.08	–46.70	–62.07	–15.85	0.24	–55.33	–40.34	–40.77
D24	–18.77	–21.00	–65.73	–34.24	–61.79	–28.88	0.68	–52.93	–37.36	–37.21
D25	–0.58	–4.57	–23.30	–14.66	–20.77	–4.26	–1.33	–14.78	–9.88	–11.76
D26	–8.91	–1.70	–9.95	–5.46	–7.76	–10.37	0.43	–7.25	–4.62	–4.18
D27	–7.09	–16.74	–42.60	–20.74	–42.57	–15.53	–11.61	–23.53	–8.65	–23.72
D28	–8.52	–3.07	–16.49	–9.58	–13.70	–7.11	0.69	–5.35	–3.71	–2.91
D29	2.08	2.52	–14.34	–12.72	–9.70	–10.79	8.46	–25.57	–23.62	–13.22
D30	–3.42	–0.10	–38.35	–28.62	–29.25	–19.91	15.10	–41.91	–39.27	–20.65
D31	–30.10	39.02	–80.23	–82.56	–34.07	–41.35	35.36	–64.90	–67.34	–23.31
D32	4.81	2.67	–13.99	–12.85	–9.64	–1.73	0.56	–6.37	–5.00	–4.37
D33	2.53	–1.42	–12.90	–9.14	–11.11	5.06	4.62	–1.70	–4.82	1.03
D34	–19.84	–15.87	–33.39	–12.91	–33.52	–27.08	–6.68	–28.38	–14.22	–23.10
D35	3177.00	–1.00	–968.00	–1084.66	–1095.68	3211.00	–35.00	–1053.00	–1130.98	–1186.27

et al. (2019) with GNSS and UAV photogrammetry were converted to the satellite line of sight (Table 2). For this conversion, surface deformations were expressed in three dimensions in the east, north, and height directions as $D = (de, d, dup)^T$, and the deformation vector was converted into the d_{LOS} (line of sight) direction using the Equation 1.

$$d_{LOS}=S^T.D \quad (1)$$

$$s=(-cos\theta sin\phi \; sin\phi sin\phi \; cos\phi)^T \quad (2)$$

Here, d_{LOS}, s, and D refer to displacements in the satellite line of sight direction, satellite unit vector, and three-dimensional surface deformations, respectively. In Equation 2, the satellite unit vector is defined in detail.

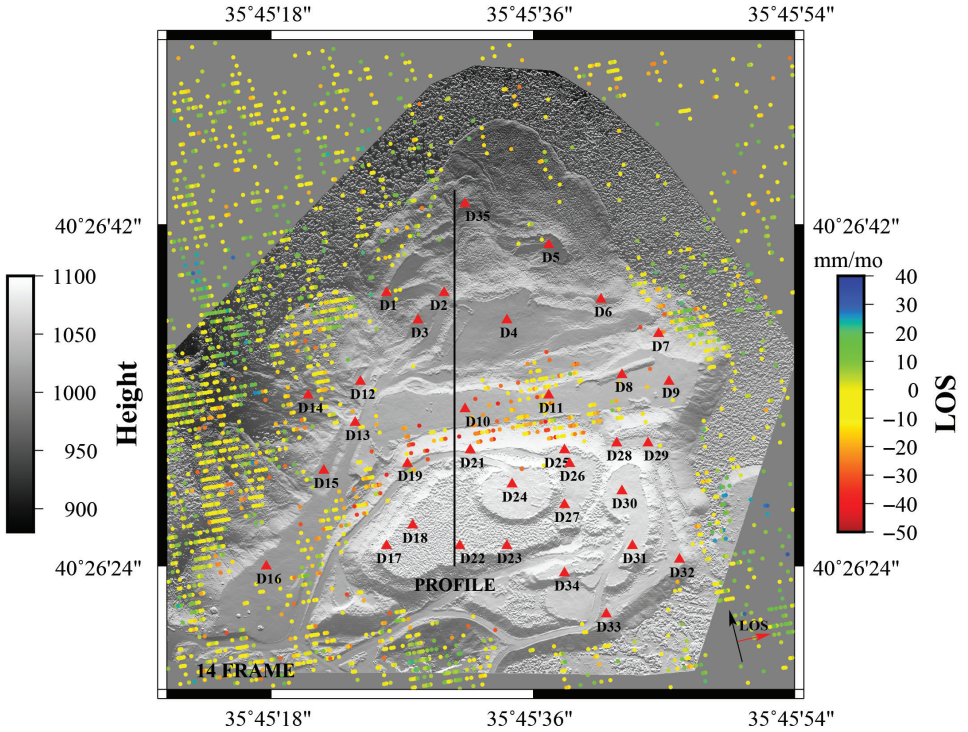

Figure 4. Motion velocities in the satellite line of sight direction obtained by evaluating Sentinel-1A images with 14 track number [▲: Hastaoğlu et al. (2019) deformation monitoring points].

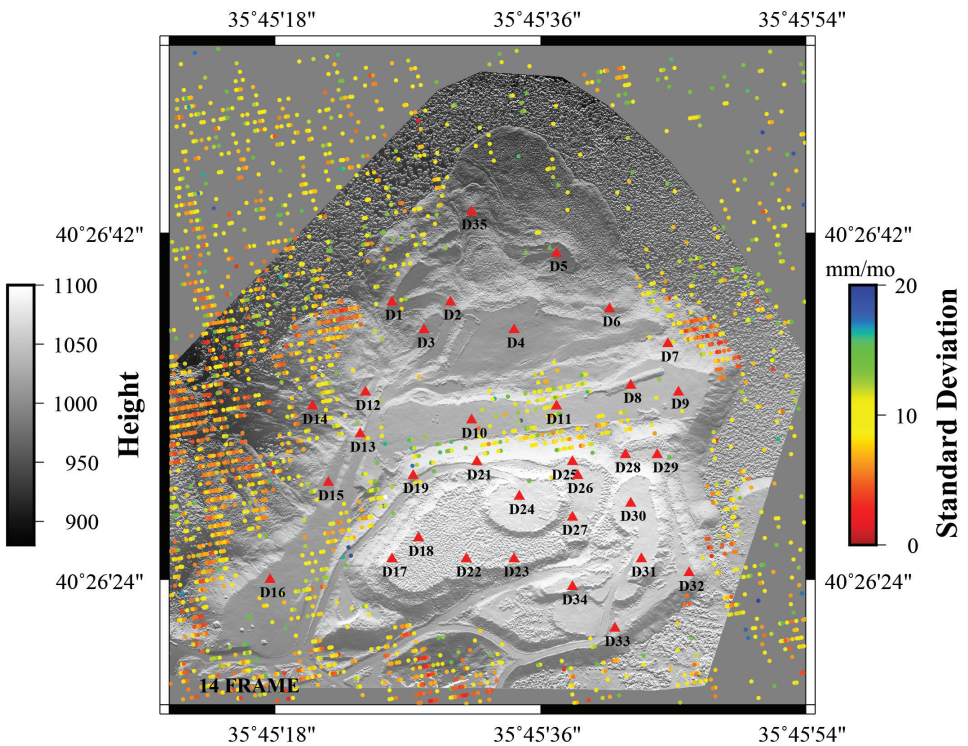

Figure 5. Standard deviations of the motion velocities in the satellite line of sight direction obtained by evaluating Sentinel-1A images with 14 track number [▲: Hastaoğlu et al. (2019) deformation monitoring points].

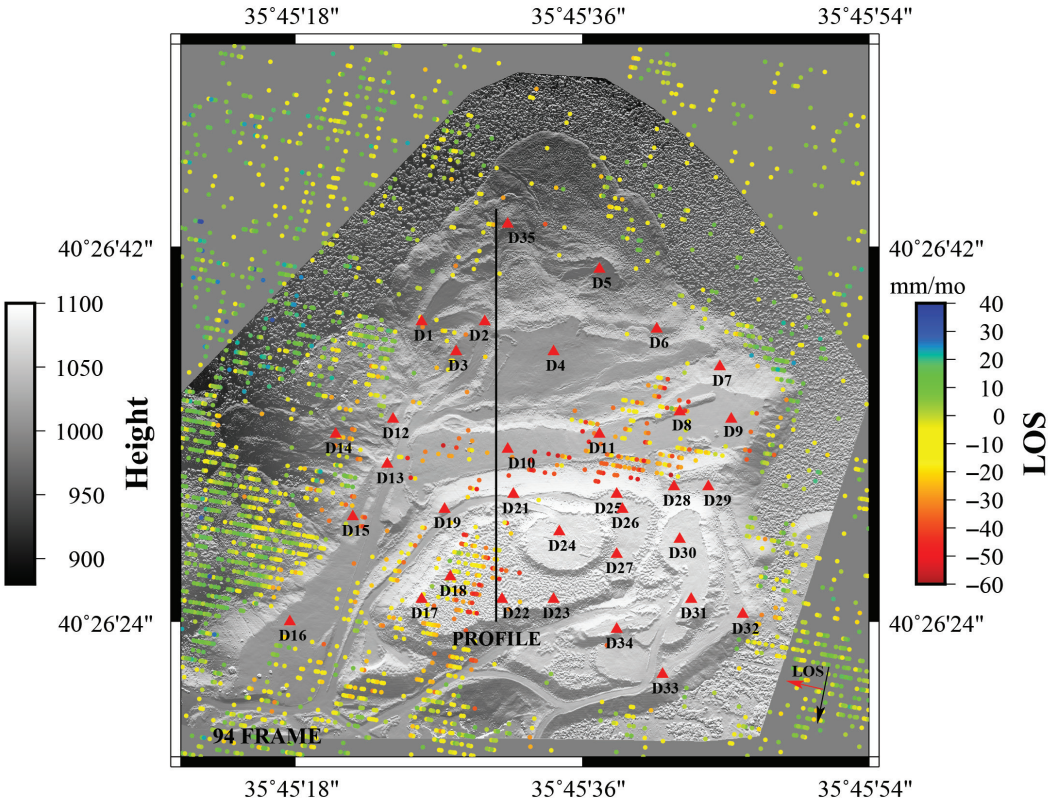

Figure 6. Motion velocities in the satellite line of sight direction obtained by evaluating Sentinel-1A images with 94 track number [▲: Hastaoğlu et al. (2019) deformation monitoring points].

Here, for the descending and ascending transition, q is the heading angle, and f is the incidence angle (Arikan et al., 2010; Hastaoglu, 2016; Fuhrmann and Garthwaite, 2019; Ezquerro et al., 2020).

3. Result and discussion

The results of this study obtained by PSI technique were generally coherent with the GNSS and UAV photogrammetry results (Hastaoğlu et al., 2019). However, different results were found from the GNSS and UAV photogrammetry (Hastaoğlu et al., 2019) in the areas where bench geometry (height, width, inclination) changed along with the ongoing dumps and frequently changing surface topography due to these dumps. Especially in the study conducted by Hastaoğlu et al. (2019), the displacement of approximately 3 m in the horizontal direction / 1 m in the vertical direction determined at point D35 could not be revealed by the PSI technique.

It is seen that according to the values in Table 2, the vertical velocities of GNSS approache approximately 80% of LOS velocities. In the images with 14 track number, q heading angle and f incidence angle are given as 350.2316° and 40.72°, respectively. In the images with 94 track number, q heading angle and f incidence angle are given as 189.9254° and 39.56°, respectively. Accordingly, when Equations 1 and 2 were used, the unit vector (–0.62 –0.11 0.78) was obtained for the frame with 14 track number, and the unit vector (0.62 –0.10 0.78) was obtained for the frame with 94 track number. In this case, the radar could detect 62%, 11%, and 78% of the east-west, north-south, and up-down movements in the frame with 14 track number, respectively, and 62%, 10%, and 78% of them in the frame with 94 track number. When the unit vector values (11%, 10%) were examined, the radar appeared to be insensitive to movements in the direction of measurement, in other words, in the north-south direction. Furthermore, while the detection of movements from west to east within the frame with 14 track number was 62%, it was totally opposite in the frame with 94 track number, in other words, movements from east to west were detected. When Table 2 was examined, it was observed that most of the deformations obtained from GNSS and UAV were high in the north direction. These deformations were also revealed by the PSI technique. However, their amounts were found to be lower. As mentioned above, one of the most important reasons of this situation was the north-south directional movements which could only be detected by around 11%

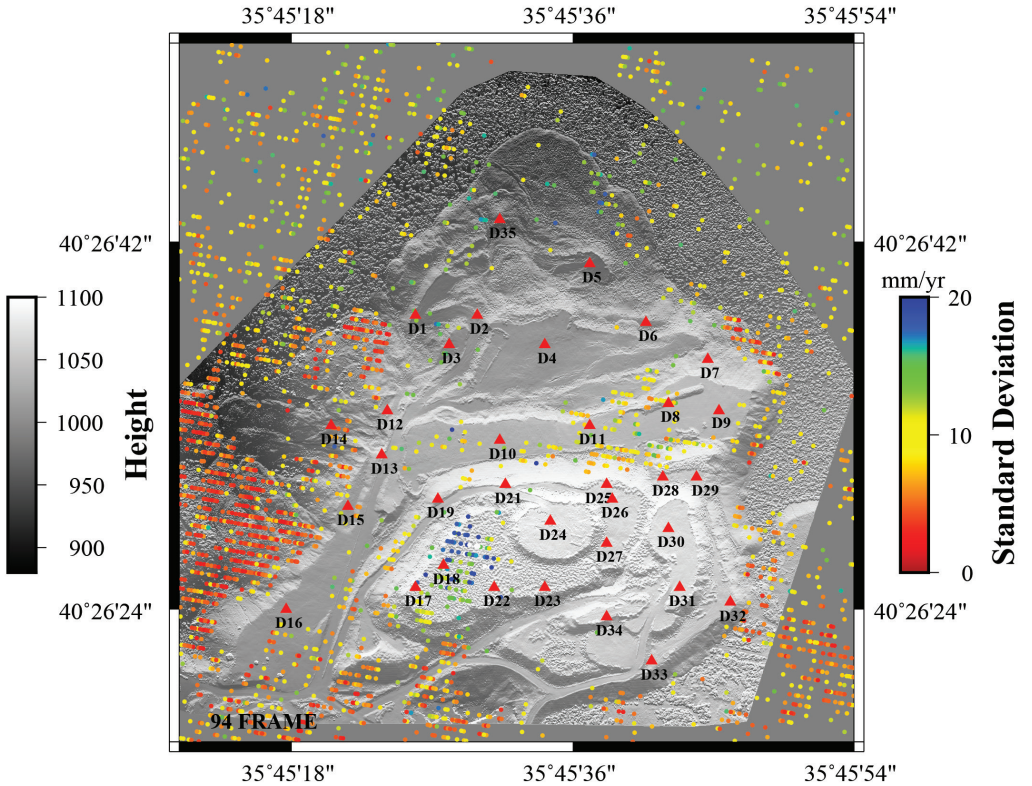

Figure 7. Standard deviations of the motion velocities in the satellite line of sight direction obtained by evaluating Sentinel-1A images with 94 track number [▲: Hastaoğlu et al. (2019) deformation monitoring points].

with the PSI technique. For all points especially at point D35, this can be considered as one of the reasons of failure of deformation determination.

Upon examining Table 2, it was observed that there was a displacement of approximately 3 m in the horizontal direction / 1 m in the vertical direction at point D35 according to four periods GNSS and three periods UAV measurements. According to the study conducted by Hastaoğlu et al. (2019), it was stated that this change occurred suddenly between the 1st and 2nd periods (between 12 July and 27 July) and this movement (9.4 cm in the horizontal direction / 4.2 cm in the vertical direction) was stationary in the subsequent periods (from 27 July to 2 September) compared to the previous periods. In this study, evaluations performed by the PSI technique, such a displacement could not be detected, especially in the time period during which deformation was high. In order to reveal what else this situation may have resulted from, detailed studies stated below were also conducted.

Firstly, the time series of two different points falling close to the point D35 were analyzed (Figures 8 and 9). When these points were examined, high displacements at point D35 could not be obtained. The maximum LOS velocity determined in the PSI evaluations performed around this point was 30 mm/mo. Furthermore, it was observed that LOS velocities at PS points were small even while the displacement at and around point D35 was maximum.

Afterward, a profile (Figures 4 and 6) was passed through a line of approximately 450 m to cover point D35, where the deformation was the highest. In this profile given in Figures 10 and 11, the LOS velocities obtained by the PSI technique, the deformation points used in GNSS and UAV photogrammetry, and also the DSM (digital surface model) obtained from 3 different periods acquired as a result of UAV photogrammetry are shown two-dimensionally. When Figures 10 and 11 were examined, it appeared that PS points were few in areas where inclination was high, which revealed the importance of the orbit of SAR satellites (descending or ascending) in inclined regions, especially in the PSI technique, and the direction of deformation development in the region.

4. Conclusions and recommendations

An unexpected ground motion has the potential to endanger life and to destroy equipment and property. Therefore, surface deformations due to mining should be monitored, and measures for the prevention of slope

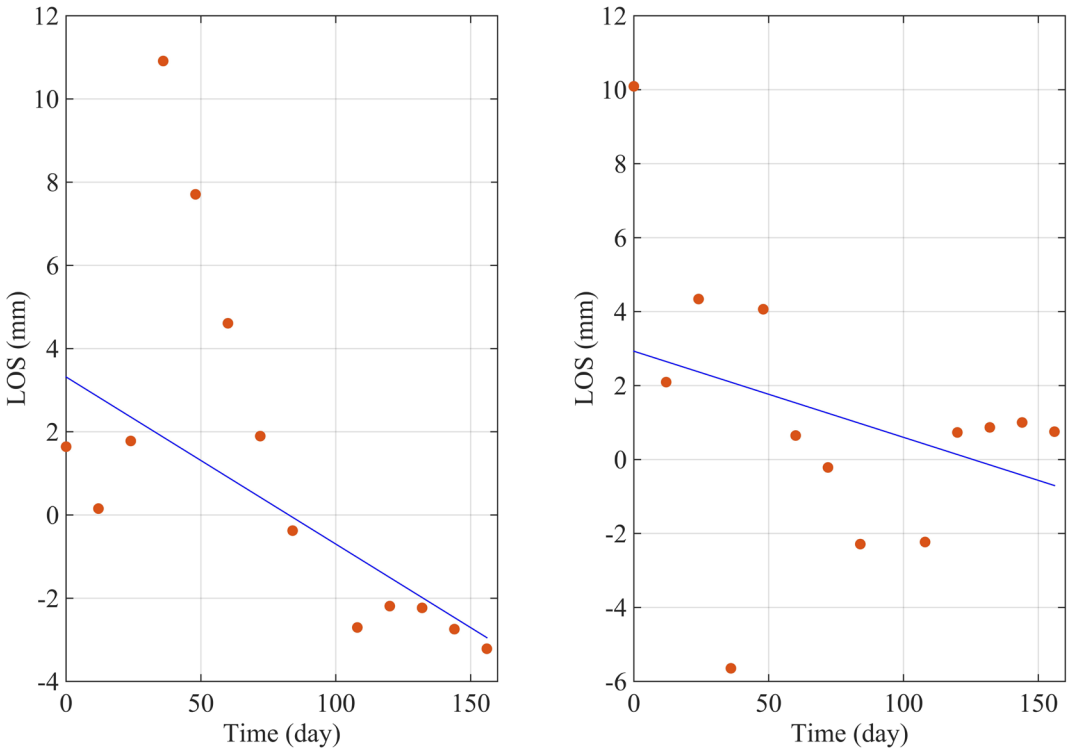

Figure 8. Time series of PS points around point D35 obtained by evaluating the satellite images with 14 track number (PS point 1; Longitude: 35.7578 Latitude: 40.4452, PS point 2; Longitude: 35.7579 Latitude: 40.4451).

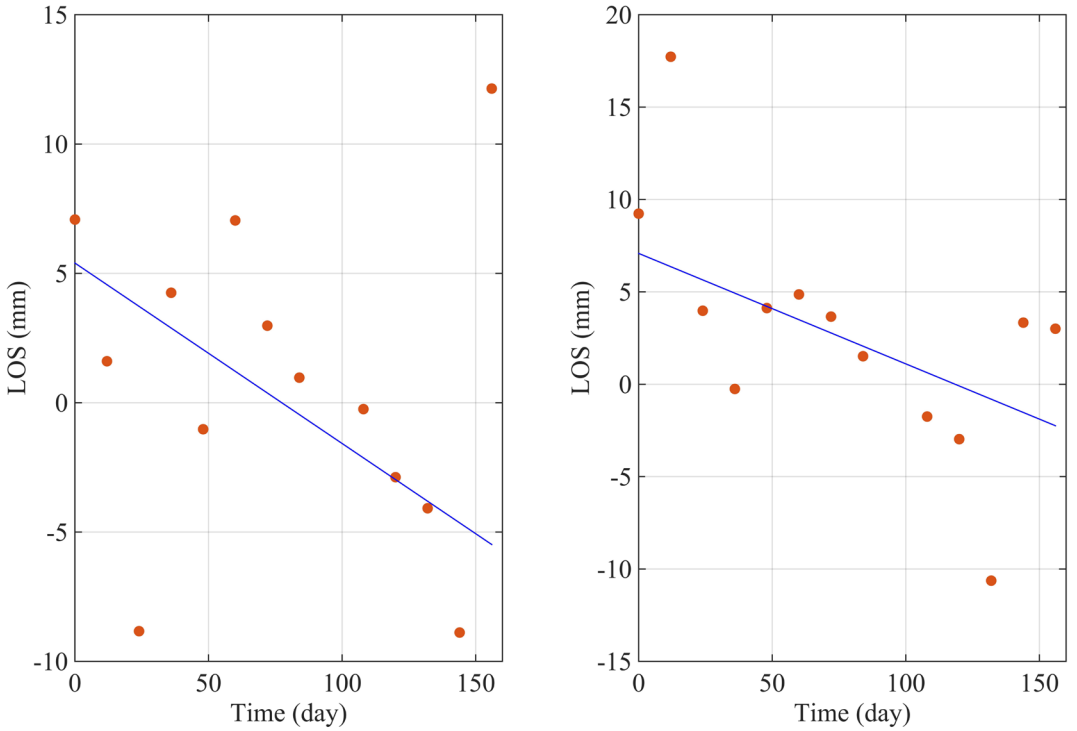

Figure 9. Time series of PS points around point D35 obtained by evaluating the satellite images with 94 track number (PS point 1; Longitude: 35.7596 Latitude: 40.4451, PS point 2; Longitude: 35.7593 Latitude: 40.4452).

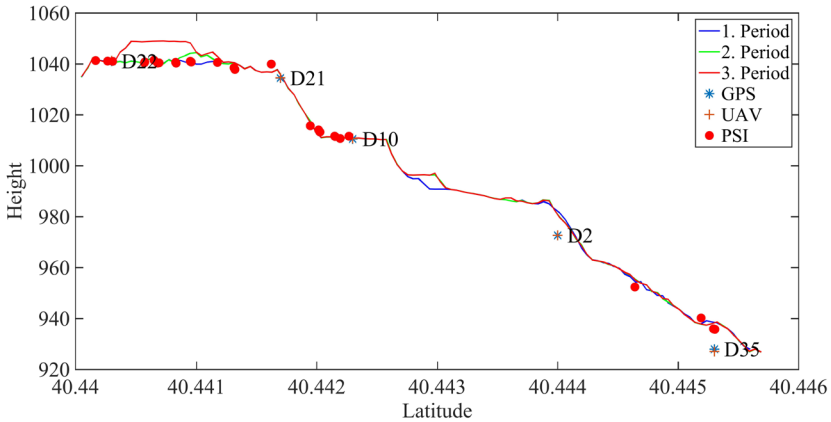

Figure 10. Profile covering the point D35 at the dump site (LOS velocities obtained by the conversion of GNSS and UAV photogrammetry points to LOS velocities according to the descending orbit data and by the evaluation of satellite images in this orbit).

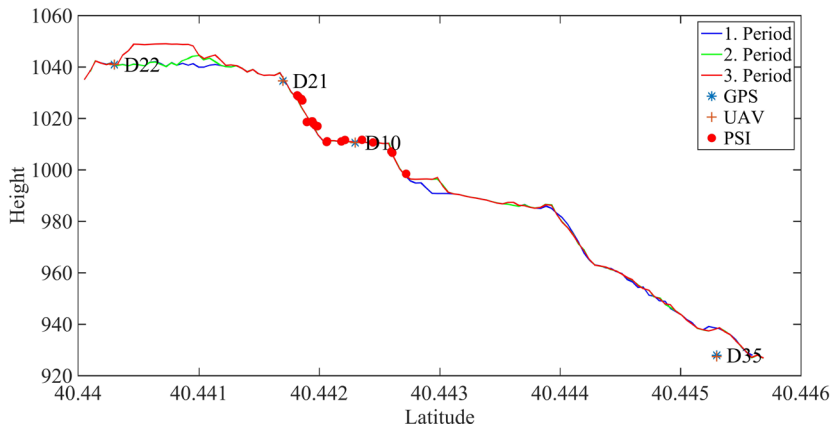

Figure 11. Profile covering the point D35 at the dump site (LOS velocities obtained by the conversion of GNSS and UAV photogrammetry points to LOS velocities according to the ascending orbit data and by the evaluation of satellite images in this orbit).

failures should be carried out. The monitoring of surface deformations caused by mining activities with traditional tools could not be easy and practical. Useful and practical results could be obtained by using new technologies and new types of measurement in monitoring studies. In this scope, the PSI technique, which uses the Sentinel-1 database, provides a state of the art solution for monitoring the advance of of mining activities.

Major deformations at the dump site occurred in the north-south direction (Table 2). Satellite radar images were used in two different orbits for the study area, and it was determined that these satellites could detect only 11% of the deformations in the north-south direction. Therefore, the direction of the deformation extension is an important factor in the PSI technique for the determination of actual deformation amounts. While deformations occurred in slow motions of long time could be found out by the PSI technique, a displacement that occurred instantly in a short time could not be determined by PS points (Figures 8 and 9). This result revealed the importance of time between periodic satellite radar images in the determination of rapid and sudden movements by the PSI technique. The deformation of D35 and it is around occurred in an area of 140 m ´ 250 m and had a volume of approximately 343 m^3 (Gül et al., 2020). Since the resolutions (5 m ´ 20 m) of the Sentinel-1A images used in this study, it was thought that one of the reasons of no detection for displacements at D35 point and around.

PS point number and frequency are the most important factors for accuracy during the determination of deformation by the PSI technique. The overall slope angle was approximately 17° in the region with high deformation (Figures 10 and 11). Sufficient PS points could not be detected in this region since the slope inclination was high, which can be the indication of relation between the number of PS points in the PSI technique and the topographic inclination.

While monitoring and determination of deformations at mining sites by the PSI technique, it was observed that the changing intense of topography due to mining activities affected the results negatively. Sudden failures occured in the area where deformation monitoring studies were conducted with satellite images could not be detected using the PSI technique. In these cases, deformation monitoring should be supported with additional images or intermediate measurements to increase temporal and spatial resolution or with other approaches to increase the number of PS points such as the placement of reflectors, especially in areas with high inclination.

Acknowledgments

We would like to thank GEOMINE R&D Software Company, which provided support to this study, and its employees. This study was supported by KOSGEB (Sivas, Turkey) in accordance with the decision no. 1 and numbered 2017-587-2 within the scope of R & D, Innovation and Industrial Application Support Program. MATLAB software used in this study are licensed by Sivas Cumhuriyet University. GMT (Wessel et al., 2013) software was used for the map drawings. Interferometric data were processed using the public domain SAR processor SNAP, StaMPS.

References

Akcin H, Kutoglu SH, Degucci T (2007). Integrating GPS and SAR: monitoring coal-field subsidence. GIM International Journal 21 (11): 41-45.

Al-Rawabdeh A, He F, Moussa A, El-Sheimy N, Habib A (2016). Using an unmanned aerial vehicle-based digital imaging system to derive a 3D point cloud for landslide scarp recognition. Remote Sensing 8 (2): 95. doi: 10.3390/rs8020095

Arikan M, Hooper A, Hanssen R (2010). Radar time series analysis over West Anatolia. In: Lacoste Francis H (editor). Fringe 2009 Proceedings. ESA SP 677. Noordwijk, Netherlands: ESA, pp. 1-6.

Bozzano F, Esposito C, Franchi S, Mazzanti P, Perissin D et al. (2015). Understanding the subsidence process of a quaternary plain by combining geological and hydrogeological modelling with satellite InSAR data: The Acque Albule Plain case study. Remote Sensing of Environment 168: 219-238. doi: 10.1016/j.rse.2015.07.010

Canuti P, Casagli N, Ermini L, Fanti R, Farina P (2004). Landslide activity as a geoindicator in Italy: significance and new perspectives from remote sensing. Environmental Geology 45 (7): 907-919. doi: 10.1007/s00254-003-0952-5

Colesanti C, Ferretti A, Novali F, Prati C, Rocca F (2003a). SAR monitoring of progressive and seasonal ground deformation using the permanent scatterers technique. IEEE Transactions on Geoscience and Remote Sensing 41 (7): 1685-1701. doi: 10.1109/TGRS.2003.813278

Colesanti C, Ferretti A, Prati C, Rocca F (2003b). Monitoring landslides and tectonic motions with the Permanent Scatterers Technique. Engineering Geology 68 (1-2): 3-14. doi: 10.1016/S0013-7952(02)00195-3

Colesanti C, Mouelic SL, Bennani M, Raucoules D, Carnec C et al. (2005). Detection of mining related ground instabilities using the Permanent Scatterers technique—a case study in the east of France. International Journal of Remote Sensing 26 (1): 201-207. doi: 10.1080/0143116042000274069

Colesanti C, Wasowski J (2004). Satellite SAR interferometry for wide-area slope hazard detection and site-specific monitoring of slow landslides. In: Proceedings of the Ninth International Symposium on Landslides; Rio de Janeiro, Brazil. pp. 795-802.

Deffontaines B, Chang KJ, Champenois J, Fruneau B, Pathier E et al. (2016). Active interseismic shallow deformation of the Pingting terraces (Longitudinal Valley–Eastern Taiwan) from UAV high-resolution topographic data combined with InSAR time series. Geomatics, Natural Hazards and Risk 8 (1): 120-136. doi: 10.1080/19475705.2016.1181678

Eker R, Aydın A, Hübl J (2018). Unmanned aerial vehicle (UAV)-based monitoring of a landslide: Gallenzerkogel landslide (Ybbs-Lower Austria) case study. Environmental Monitoring and Assessment 190 (1): 28. doi: 10.1007/s10661-017-6402-8

Ezquerro P, Del Soldato M, Solari L, Tomás R, Raspini F et al. (2020). Vulnerability assessment of buildings due to land subsidence using InSAR data in the ancient historical city of Pistoia (Italy). Sensors 20 (10): 2749. doi: 10.3390/s20102749

Ferretti A, Prati C, Rocca F (2001). Permanent scatterers in SAR interferometry. IEEE Transactions on Geoscience and Remote Sensing 39 (1): 8-20. doi: 10.1109/36.898661

Ferretti A, Prati C, Rocca F, Casagli N, Farina P et al. (2005). Permanent Scatterers technology: a powerful state of the art tool for historic and future monitoring of landslides and other terrain instability phenomena. In: International Conference on Landslide Risk Management; Vancouver, Canada. pp. 1-9.

Ferrigno F, Gigli G, Fanti R, Intrieri E, Casagli N (2017). GB-InSAR monitoring and observational method for landslide emergency management: the Montaguto earthflow (AV, Italy). Natural Hazards & Earth System Sciences 17 (10): 845–860. doi: 10.5194/nhess-17-845-2017

Fuhrmann T, Garthwaite MC (2019). Resolving three-dimensional surface motion with InSAR: Constraints from multi-geometry data fusion. Remote Sensing 11 (3): 241. doi: 10.3390/rs11030241

Graniczny M, Colombo D, Kowalski Z, Przyłucka M, Zdanowski A (2015). New results on ground deformation in the Upper Silesian Coal Basin (southern Poland) obtained during the DORIS Project (EU-FP 7). Pure and Applied Geophysics 172: 3029-3042. doi: 10.1007/s00024-014-0908-6

Gül Y, Hastaoğlu KÖ, Poyraz F (2020). Using the GNSS method assisted with UAV photogrammetry to monitor and determine deformations of a dump site of three open-pit marble mines in Eliktekke region, Amasya province, Turkey. Environmental Earth Sciences 79 (11): 1-20. doi: 10.1007/s12665-020-08959-8

Hastaoglu KO (2016). Comparing the results of PSInSAR and GNSS on slow motion landslides, Koyulhisar, Turkey. Geomatics, Natural Hazards and Risk 7 (2): 786-803. doi: 10.1080/19475705.2014.978822

Hastaoğlu KÖ, Gül Y, Poyraz F, Kara BC (2019). Monitoring 3D areal displacements by a new methodology and software using UAV photogrammetry. International Journal of Applied Earth Observation and Geoinformation, 83: 101916. doi: 10.1016/j.jag.2019.101916

Hooper A, Bekaert D, Hussain E, Spaans K (2018). StaMPS/MTI Manual (Version 4.1b). Leeds, UK: University of Leeds School of Earth and Environment, p. 41.

Hooper A, Segall P, Zebker H (2007). Persistent scatterer interferometric synthetic aperture radar for crustal deformation analysis, with application to Volca´n Alcedo, Gala´pagos. Journal of Geophysical Research 112: B07407. doi: 10.1029/2006JB004763

Jakóbczyk J, Cała M, Stopkowicz A (2015). What were the reasons for the rapid landslide occurrence in "Piaseczno" open pit?–analysis of the landslide process. Studia Geotechnica et Mechanica 37 (1): 25-35. doi: 10.1515/sgem-2015-0004

Jarosz A, Wanke D (2004). Use of InSAR for monitoring of mining deformations. In: Lacoste H (editor). Fringe 2003 Proceedings. ESA SP-550. Frascati, Italy: ESA, pp. 283-288.

Kristensen L, Rivolta C, Dehls J, Blikra LH (2013). GB-InSAR measurement at the Åknes rockslide, Norway. Italian Journal of Engineering Geology and Environment - Book Series 6: 339-348. doi: 10.4408/IJEGE.2013-06.B-32

Meisina C, Zucca F, Fossati D, Ceriani M, Allievi J (2006). Ground deformation monitoring by using the permanent scatterers technique: the example of the Oltrepo Pavese (Lombardia, Italy). Engineering Geology 88 (3-4): 240-259. doi: 10.1016/j.enggeo.2006.09.010

Mora O, Álvarez I, Amor Herrera E (2013). Slope stability study in open pit and underground mines by means of forensic analysis and radar interferometry. In: International Symposium on Slope Stability in Open Pit Mining and Civil Engineering, Australian Centre for Geomechanics; Perth, Australia. pp. 1021-1032.

Niethammer U, James MR, Rothmund S, Travelletti J, Joswig M (2012). UAV-based remote sensing of the Super-Sauze landslide: evaluation and results. Engineering Geology 128: 2-11. doi: 10.1016/j.enggeo.2011.03.012

Paradella WR, Ferretti A, Mura JC, Colombo D, Gama FF et al. (2015). Mapping surface deformation in open pit iron mines of Carajás Province (Amazon Region) using an integrated SAR analysis. Engineering Geology 193: 61-78. doi: 10.1016/j.enggeo.2015.04.015

Peppa MV, Mills JP, Moore P, Miller PE, Chambers JE (2017). Brief communication: landslide motion from cross correlation of UAV-derived morphological attributes. Natural Hazards and Earth System Sciences 17 (12): 2143-2150. doi: 10.5194/nhess-17-2143-2017

Perski Z, Hanssen R, Wojcik A, Wojciechowski T (2009). InSAR analyses of terrain deformation near the Wieliczka Salt Mine, Poland. Engineering Geology 106 (1-2): 58-67. doi: 10.1016/j.enggeo.2009.02.014

Pinto CdA, Paradella WR, Mura JC, Gama FF, Dos Santos AR et al. (2014). Results of the application of persistent scatterers interferometry for surface displacements monitoring in the Azul open pit manganese mine (Carajás Province, Amazon region) using TerraSAR-X data. Proceedings Volume 9245, Earth Resources and Environmental Remote Sensing/GIS Applications V: 92451K. doi: 10.1117/12.2067233

Pinto CdA, Paradella WR, Mura JC, Gama FF, Dos Santos AR et al. (2015). Applying persistent scatterer interferometry for surface displacement mapping in the Azul open pit manganese mine (Amazon region) with TerraSAR-X StripMap data. Journal of Applied Remote Sensing 9: 095978. doi: 10.1117/1.JRS.9.095978

Ren H, Zhao Y, Xiao W, Hu Z (2019). A review of UAV monitoring in mining areas: current status and future perspectives. International Journal of Coal Science & Technology 6 (3): 320-333. doi: 10.1007/s40789-019-00264-5

Temporim FA, Gama FF, Mura JC, Paradella WR, Silva GG (2017). Application of persistent scatterers interferometry for surface displacements monitoring in N5E open pit iron mine using TerraSAR-X data, in Carajás Province, Amazon region. Brazilian Journal of Geology 47 (2): 225-235. doi: 10.1590/2317-4889201720170006

Tong X, Liu X, Chen P, Liu S, Luan K et al. (2015) Integration of UAV-based photogrammetry and terrestrial laser scanning for the three-dimensional mapping and monitoring of open-pit mine areas. Remote Sensing 7 (6): 6635-6662. doi: 10.3390/rs70606635

Wessel P, Smith WHF, Scharroo R, Luis J, Wobbe F (2013). Generic mapping tools: improved version released. EOS Transactions American Geophysical Union 94 (45): 409-410. doi: 10.1002/2013EO450001